

RAINBOW Organic Solar Cells: Implementing Spectral Splitting in Lateral Multi-Junction Architectures

Martí Gibert-Roca, Miquel Casademont-Viñas, Quan Liu, Koen Vandewal, Alejandro R. Goñi, and Mariano Campoy-Quiles*

While multi-junction geometries have the potential to boost the efficiency of organic solar cells, the experimental gains yet obtained are still very modest. This work proposes an alternative spectral splitting device concept in which various individual semiconducting junctions with cascading bandgaps are laid side by side, thus the name RAINBOW. Each lateral sub-cell receives a fraction of the spectrum that closely matches the main absorption band of the given semiconductor. Here, simulations are used to identify the important material and device properties of each RAINBOW sub-cell. Using the resulting design rules, three systems are selected, with narrow, medium, and wide effective bandgaps, and their potential as sub-cells in this geometry is experimentally investigated. With the aid of a custom-built setup that generates spectrally spread sunlight on demand, the simulations are experimentally validated, showing that this geometry can lead to a reduction in thermalization losses and an improvement in light harvesting, which results in a relative improvement in efficiency of 46.6% with respect to the best sub-cell. Finally, a working proof-of-concept monolithic device consisting of two sub-cells deposited from solution on the same substrate is fabricated, thus demonstrating the feasibility and the potential of the RAINBOW solar cell concept.

1. Introduction

Single-junction solar cell efficiencies are limited by absorption and thermalization losses to a maximum theoretical efficiency of $\approx 33\%$.^[1,2] This limit arises from the spectral mismatch between the bandgap of the semiconducting junction and the solar spectrum; where photons with energies $E < E_g$ pass through the material unabsorbed and photons with energies $E > E_g$ dissipate their excess energy as heat, limiting the theoretical maximum efficiency on a fundamental level.

So far, the most promising strategy to overcome this fundamental limitation consists of combining multiple semiconducting junctions, with different bandgaps, that attempt to match the energy of incoming photons, so to minimize thermalization losses and maximize absorption.^[3,4] Up to date, the most common implementation of such multi-junction solar cells consists of vertically stacked devices. In this configuration, the topmost junction absorbs the shortest wavelength

range, while unabsorbed photons, with $E < E_g$, go through to the next sub-cell where this partial spectral absorption is repeated, resulting in a complementary absorption along the entire multi-junction stack (**Figure 1a**).^[3,5–11] This strategy yields a theoretical maximum efficiency, with infinite junctions, of 68% under AM 1.5G illumination, and 86% with solar concentration, resulting in a promising alternative for large-scale power generation.^[3,4]


The catalog of organic semiconductors for photovoltaic applications has expanded greatly over the past decade leading to single junction efficiencies above 19%.^[3,12–16] Despite the large material library available, with widely varying bandgaps, organic multi-junction geometries have, thus far, shown modest success, not yielding more than a few percentages improvement over the best sub-cell efficiency.^[16] This is, in part, due to the difficulty to fabricate such geometries from solution^[17,18] and further complicated by the need for current matching between sub-cells in two terminal devices,^[19,20] as well as the availability and implementation of transparent interconnecting layers (ICLs).

An alternative configuration for multi-junction cells is the spectral beam splitting geometry.^[21,22] This involves spectrally separating the solar spectrum and redirecting the spectral

M. Gibert-Roca, M. Casademont-Viñas, M. Campoy-Quiles
Dept. of Nanostructured Materials
Institut de Ciència de Materials de Barcelona (ICMAB-CSIC)
E-08193 Cerdanyola del Vallès, Spain
E-mail: mcampoy@icmab.es

Q. Liu, K. Vandewal
IMO-IMOMECE
Hasselt University
Wetenschapspark 1, BE3590 Diepenbeek, Belgium

A. R. Goñi
ICREA
Passeig Lluís Companys 23
E-08010 Barcelona, Spain

 The ORCID identification number(s) for the author(s) of this article can be found under <https://doi.org/10.1002/adma.202212226>

© 2023 The Authors. Advanced Materials published by Wiley-VCH GmbH. This is an open access article under the terms of the Creative Commons Attribution License, which permits use, distribution and reproduction in any medium, provided the original work is properly cited.

DOI: 10.1002/adma.202212226

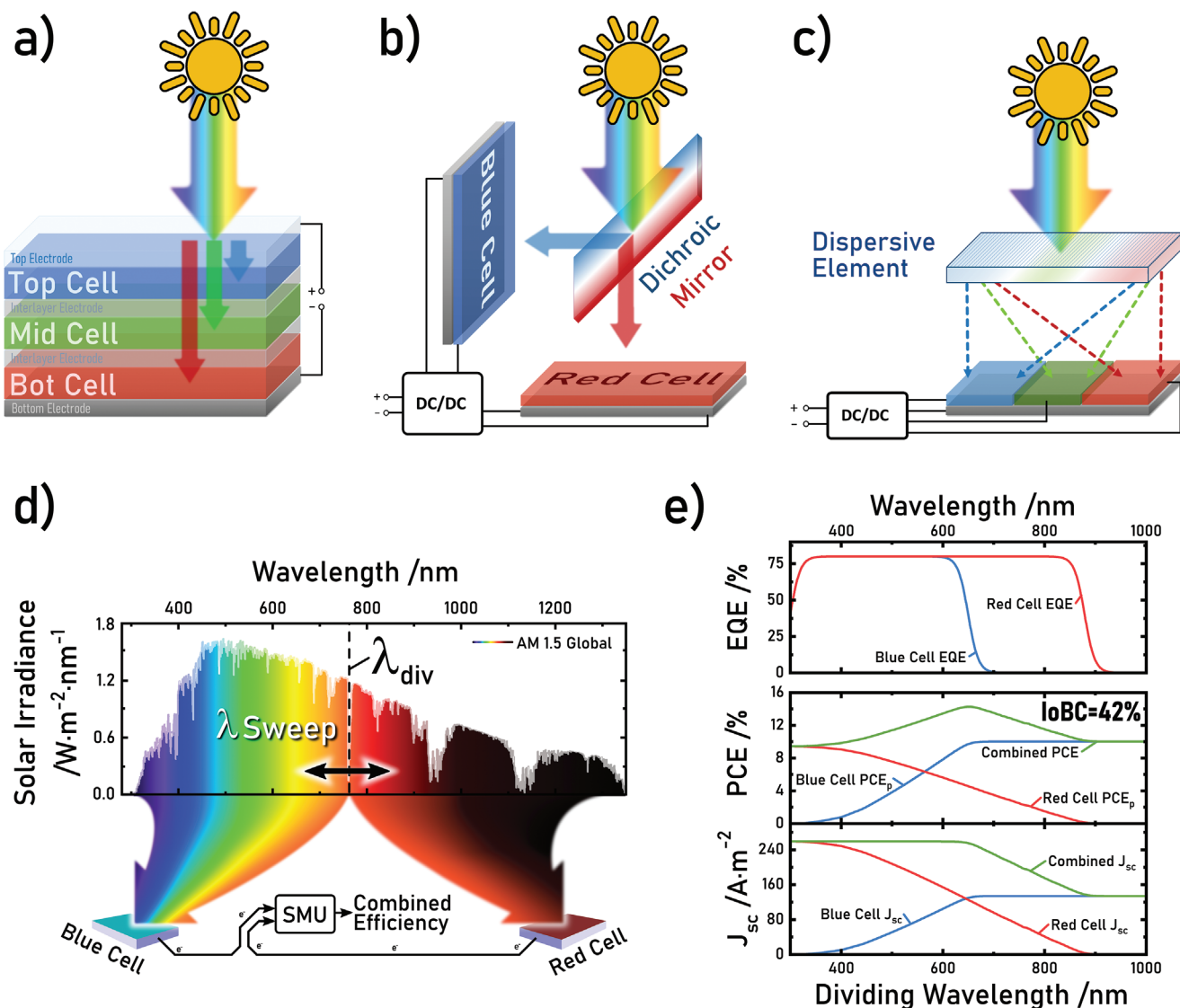


Figure 1. a) Stacked, series connected multi-junction configuration. b) Solar spectral splitting tandem configuration with a dichroic mirror as the light redirecting optical element. c) RAINBOW multi-junction configuration with a dispersive element that performs the spectral splitting. d) Schematic representation of a two sub-cell RAINBOW measurement, where the solar spectrum is divided in two complementary parts by a dividing wavelength, which is swept across the spectrum to evaluate the optimal value for any given RAINBOW material combination. e) RAINBOW combination performance graph, with ideal EQE curves for each individual sub-cell (top), and the partial and combined PCE (middle) and J_{sc} (bottom) curves as a function of the dividing wavelength.

fractions to different sub-cells,^[23] as shown in Figure 1b for two sub-cells. This approach has yielded promising results in various systems, such as high efficiency III–V material multi-junctions,^[24,25] hybrid inorganic perovskite multi-junction solar cells,^[26,27] as well as hybrid silicon thermal absorbers^[28–30] and thermoelectrics.^[31–33] Having physically separated cells makes fabrication simple, and sub-cell connection straightforward. The implementation of such systems has, however, proven to be rather cumbersome, as the most common configuration consists in placing each sub-cell at 90°, with a dichroic mirror at 45° spectrally redistributing sunlight, resulting in an awkward form factor that gets significantly more complex when increasing the junction count.^[21]

In this work, we devise an alternative beam splitting configuration, consisting of a forward wavelength spreading element located over a horizontal stack multi-junction solar cell, so-called RAINBOW solar cell, as illustrated in Figure 1c. The RAINBOW approach, being a monolithic in-plane manufacturing solution, can be based on deposition techniques that are considered already advanced.^[34–37] On the other hand, the lateral distribution of each sub-cell allows for an easy implementation of electrically independent contacts, eliminating the need for current or voltage matching on a device level.^[38,39] Finally, a RAINBOW cell uses the same amount of material for electrodes, active layer, transport layers, and substrate than a single junction cell, without significantly complicating production (see below), thus the

sustainability and cost of this architecture will be competitive, provided that the dispersive element can be manufactured easily, sustainably, and cheaply.

Given the large material catalogue and their ease of processing, we have chosen to investigate the potential of organic semiconductors in this specific geometry. It is worth noting, however, that the here introduced geometry could be used in other photovoltaic technologies provided that they exhibit a wide range of possible bandgap energies and are also suitable to be processed into stripes of different materials (either by solution processing or evaporation through a shadow mask). This would be the case for perovskites, but also for quantum dots, kesterites and more recently for oxide based photovoltaics.

Here, we have first studied this configuration from a theoretical point of view, evaluating its feasibility on a fundamental level and simulating the performance of different RAINBOW material combinations to establish design rules for sub-cell material selection. Using these rules, we have selected three systems for experimental study and implementation. As a wide-bandgap combination, we have selected, poly[(2,6-(4,8-bis(5-(2-ethylhexyl-3-fluoro)thiophen-2-yl)-benzo[1,2-b:4,5-b']dithiophene)-alt-(5,5-(1',3'-di-2-thienyl-5',7'-bis(2-ethylhexyl)benzo[1',2'-c:4',5'-c']dithiophene-4,8-dione)] (PBDB-T-2F) donor together with 3,9-bis[5,6-dichloro-1H-indene-1,3(2H)dione]-5,5,11,11-tetrakis(4-hexylphenyl)-dithieno[2,3-d:2',3'-d']-s-indaceno[1,2-b:5,6-b']dithiophene (IO-4Cl) as the acceptor. For the intermediate material system, we have selected PBDB-T-2F as donor and 2,2'-((2Z,2'Z)-((12,13-bis(2-ethylhexyl)-3,9-diundecyl-12,13-dihydro-[1,2,5]thiadiazolo[3,4-e]thieno[2'',3':4',5']thieno[2',3':4,5]pyrrolo[3,2-g]thieno[2',3':4,5]thieno[3,2-b]indole-2,10-diyl)bis(methanylylidene))-bis(5,6-difluoro-3-oxo-2,3-dihydro-1H-indene-2,1-diylidene))dimalononitrile (Y6) as acceptor. Finally, for the narrow gap sub-cell, we have used poly[4,8-bis(5-(2-ethylhexyl)thiophen-2-yl)benzo[1,2-b:4,5-b']dithiophene-2,6-diyl-alt-(4-(2-ethylhexyl)-3-fluorothieno[3,4-b]thiophene)-2-carboxylate-2,6-diyl)] (PTB7-Th) as donor and 2,2'-((2Z,2'Z)-(((4,4-bis(2-ethylhexyl)-4H-cyclopenta[2,1-b:3,4-b']dithiophene-2,6-diyl)bis(4-(2-ethylhexyloxy)thiophene-5,2-diyl))bis(methanylylidene))bis(5,6-difluoro-3-oxo-2,3-dihydro-1H-indene-2,1-diylidene))dimalononitrile (COTIC-4F) as acceptor. The experimental results are in good agreement with the simulations, exhibiting an efficiency increase-over-best-cell (IoBC) of up to 46.6%. Finally, we fabricated and characterized two proof-of-concept monolithic two-junction RAINBOW devices, demonstrating the feasibility of the RAINBOW solar cell concept.

2. Results and Discussion

2.1. RAINBOW Concept

The RAINBOW solar cell concept consists in two main parts: a light dispersive element and a horizontal multi-junction array. The wavelength spreading element, located above the multi-junction solar cell, spatially redistributes the solar spectrum into all its composing wavelengths. This combination results in a rainbow of colors, as shown in Figure 1c, where each sub-cell is illuminated with the optimal wavelength range, minimizing thermalization losses, while being able to absorb the majority of the solar spectrum.

This work is focused on the study of the horizontal stack multi-junction solar cell, whereas the wavelength dispersive element is discussed elsewhere.^[40] It is worth mentioning, however, that such elements have been previously reported, with multiple solutions available such as the dispersive lens proposed by Thio et al.,^[41] or the holographic solution proposed by Vorndran et al.^[42]

The main advantage of the RAINBOW configuration lies on its ability to reduce both thermalization and absorption losses, while avoiding the limitations of vertical stack manufacturing, such as defect accumulation and optical transparency loss,^[12,39] and the awkward form factor of other beam splitting geometries,^[21,22] thanks to its planar lateral deposition configuration. While the RAINBOW geometry is not as simple as a single-junction device, in this novel configuration one can increase the number of sub-cells from 2 to N junctions without changing the form factor.

To illustrate the power of the spectral splitting concept, we compare a case study of a three-junction RAINBOW cell where each sub-cell is illuminated by either the full solar spectrum or spectrally separated sunlight, dispersed by a hypothetical optical element. For the latter, the optical element ideally splits the entire solar spectrum in three regions of equal integrated spectral irradiance, each of which illuminates the corresponding sub-cell of the RAINBOW device (see Section S1, Supporting Information for details). According to the Shockley–Queisser limit, the best ideal single-junction cell would exhibit a PCE of $\approx 33\%$, whereas the RAINBOW cell would show an average PCE of 25% without spectral splitting, and close to 51% when using the dispersive optical element. The latter exhibits a net gain in both the open circuit voltage V_{oc} , due to minimization of thermalization losses in each sub-cell, and in the short circuit current J_{sc} , due to an optimized photon absorption.

2.2. Simulations

In this section, we simulate the behavior of more realistic devices as compared to the idealized case mentioned before, by using a customized model able to calculate the efficiency of RAINBOW solar cells by splitting the solar spectrum into arbitrary fractions, and redirecting them to the corresponding sub-cells. As a first approximation, inspired by previously tested beam splitting technologies like dichroic mirror beam splitting,^[21] we simulated RAINBOW systems with just two sub-cells.

To simulate the performance of the two sub-cells in these RAINBOW configurations we divide the solar spectrum in two parts: a “blue fraction” containing the shorter wavelengths, and a “red fraction” containing the longer ones. These spectral fractions are redirected to each of the two sub-cells, which are consequently named “blue cell” and “red cell,” respectively (Figure 1d). The overall performance of the RAINBOW cell greatly depends on how we divide the solar spectrum, with the dividing wavelength λ_{div} being a key parameter that condensates this idea in the simulations.

In the ideal case, for lossless sub-cells with top hat shaped external quantum efficiency (EQE) curves, the optimal λ_{div} value is expected to coincide with the bandgap of the “blue cell.” Nonetheless, in real devices with spectrally irregular EQE curves and different V_{loss} values, the optimum splitting of the illumination

spectrum should be determined case by case. For this, we sweep the dividing wavelength across the solar spectrum, changing the size of the “blue fraction” and the “red fraction” systematically, to evaluate RAINBOW performance under various spectral splitting conditions and material properties.

As an approximation to determine RAINBOW efficiency under varying illumination conditions, associated to the different spectral fractions, we calculate J_{sc} by integrating the product of the EQE and solar spectral irradiance curves according to Equation (1), where $\text{EQE}(\lambda)$ is the EQE curve, $E_{e,\lambda}(\lambda)$ is the solar spectral irradiance, $\epsilon_{ph}(\lambda)$ is the photon energy and q_e is the electron electric charge. Conveniently, by substituting the solar spectrum in Equation (1) for the “red fraction” or “blue fraction” spectrum at each dividing wavelength ($E_{e,\lambda}(\text{red}) (\lambda, \lambda_{div})$ and $E_{e,\lambda}(\text{blue}) (\lambda, \lambda_{div})$), we obtain Equations (2) and (3) from which the respective J_{sc} at every dividing wavelength can be calculated.

$$J_{sc} = \int_0^\infty \frac{E_{e,\lambda}(\lambda)}{\epsilon_{ph}(\lambda)} \text{EQE}(\lambda) q_e d\lambda \quad (1)$$

$$J_{sc(\text{blue})}(\lambda_{div}) = \int_0^\infty \frac{E_{e,\lambda}(\text{blue}) (\lambda, \lambda_{div})}{\epsilon_{ph}(\lambda)} \text{EQE}(\lambda) q_e d\lambda \quad (2)$$

$$J_{sc(\text{red})}(\lambda_{div}) = \int_0^\infty \frac{E_{e,\lambda}(\text{red}) (\lambda, \lambda_{div})}{\epsilon_{ph}(\lambda)} \text{EQE}(\lambda) q_e d\lambda \quad (3)$$

The resulting partial J_{sc} values can then be multiplied by the V_{oc} and the FF of each sub-cell to obtain their partial efficiency. As part of the approximation, which is supported by the measurements presented below, we assume that the V_{oc} and FF values remain constant and equivalent to those measured under AM 1.5G conditions. Taking that into account, we can calculate the partial efficiency contribution of each sub-cell with Equations (4) and (5).

$$\text{PCE}_{(\text{blue})}(\lambda_{div}) = \frac{J_{sc(\text{blue})}(\lambda_{div}) \text{FF}_{(\text{blue})} V_{oc(\text{blue})}}{E_{e,\lambda}} \quad (4)$$

$$\text{PCE}_{(\text{red})}(\lambda_{div}) = \frac{J_{sc(\text{red})}(\lambda_{div}) \text{FF}_{(\text{red})} V_{oc(\text{red})}}{E_{e,\lambda}} \quad (5)$$

As a result, this mathematical model yields a partial J_{sc} and a partial PCE value for each of the sub-cells, normalized against AM 1.5G input power, which can be simply added to that of another sub-cell to obtain their combined RAINBOW performance, as shown in Figure 1e. Note that this assumptions are valid when sub-cells are connected externally (in this case, a four terminal device), and this model only works under the condition that $E_{e,\lambda(\text{red})} + E_{e,\lambda(\text{blue})} = E_{e,\lambda}$, where we can assume partial J_{sc} and PCE to be additive magnitudes, leading to Equations (6) and (7).

$$J_{sc,\text{comb}} = J_{sc(\text{red})} + J_{sc(\text{blue})} \quad (6)$$

$$\text{PCE}_{\text{comb}} = \text{PCE}_{(\text{red})} + \text{PCE}_{(\text{blue})} \quad (7)$$

Their combined efficiency can then be evaluated against that of the best performing RAINBOW sub-cell to obtain the figure of merit called “increase-over-best-cell” (IoBC), which re-

flects the gains in power conversion efficiency of a given multi-junction combination when matched against its best single-junction sub-cell (Equation (8)). When combined with the maximum multi-junction efficiency, these figures of merit provide a quick overview of the overall multi-junction solar cell performance.^[42]

$$\text{IoBC} = \frac{\text{PCE}_{\text{comb,max}} - \text{PCE}_{\text{max}(\text{best-sub-cell})}}{\text{PCE}_{\text{max}(\text{best-sub-cell})}} \quad (8)$$

The resulting model is able to quickly evaluate the combined performance of two different material junctions, in a RAINBOW configuration, from just their J - V and EQE curves, allowing us to determine possible RAINBOW combinations from separately manufactured sub-cells, before having to manufacture the actual RAINBOW device.

2.2.1. Ideal EQE Curves

To establish a basic set of guidelines for material combination selection in RAINBOW solar cells we first employed the model to evaluate the performance of a series of sub-cell material combinations, with idealized top hat EQE curves, sigmoid edges, and varying widths and heights. The edge of the EQE curves was used to calculate E_g , from which the V_{oc} was obtained combining the Shockley–Queisser limit and a polynomial fit from the data published in ref. [43] and the FF was assumed to be constant at 65%. These J - V parameters, along with the EQE curves, were fed into the numerical model to evaluate the RAINBOW performance of every possible ideal EQE combination. The resulting combination performance is represented by a dividing wavelength sweep graph, which shows both the EQE curves, and the combined and partial power conversion efficiency and J_{sc} of each sub-cell as a function of the dividing wavelength (see an example in Figure 1e). Further details, including a variety of examples with different representative cases, are given in Section S2, Supporting Information. From these simulations, we identify the following guidelines to maximize RAINBOW PCE:

- Low V_{oc} losses: To reduce thermalization losses, each sub-cell needs to have inherently low V_{oc} losses, particularly the blue cells. Otherwise, even with higher bandgaps, thermalization losses will not be reduced. This is similar to any other multi-junction cell.
- Similar EQE values around their respective bandgaps: In a RAINBOW configuration, each sub-cell will likely operate close to its bandgap, in the spectral region where most organic materials have their strongest absorption band. If there is a spectral region where red and blue EQEs overlap, the EQE of the blue cell should be, at least, as high as that of the red cell, otherwise, there will be a compromise between better V_{oc} and worse J_{sc} . Interestingly, in this configuration, materials should be maximum EQE matched, a condition much easier to achieve than the current matching required in series connected tandem stacks.
- High sub-cell efficiencies: Generally speaking, the combined RAINBOW efficiency is directly related to the achievable individual efficiency of each sub-cell, which must be as high as possible. However, the cell parameters for maximum combined

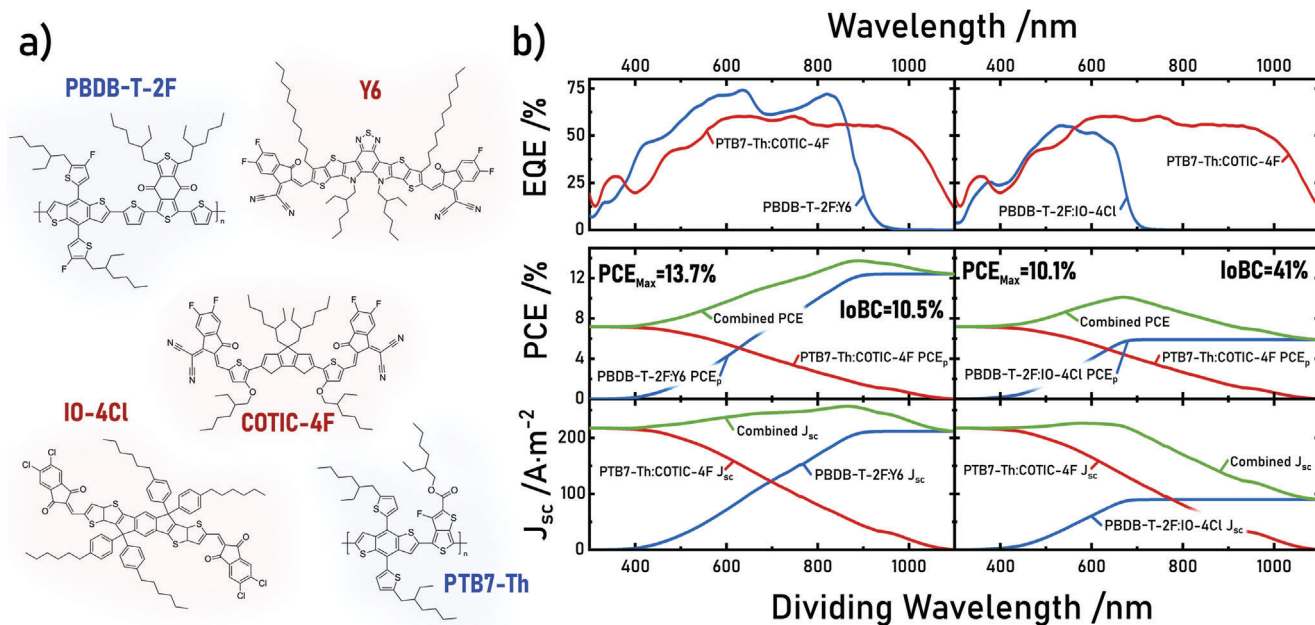


Figure 2. a) Chemical structure of PBDB-T-2F and PTB7-Th (donors) and IO-4Cl, Y6, and COTIC-4F (acceptors). b) Experimental EQE (top) and simulated combined performance graph for the two functional RAINBOW combinations; PBDB-T-2F:Y6 as blue cell and PTB7-Th:COTIC-4F as red cell (left), and PBDB-T-2F:IO-4Cl as blue cell and PTB7-Th:COTIC-4F as red cell (right).

PCE can differ from the optimal values of the individual cells. In particular, we expect that in general, optimal RAINBOW sub-cells may be thinner than their single junction counterparts. That is because each sub-cell is only illuminated around its absorption maximum, where thin films are capable of absorbing most light, with the added benefit of thinner cells exhibiting a higher FF. Compared to a tandem stack, the thickness of each cell can be optimized independently for each sub-cell, as no filtering effects occur.

Moreover, in order to maximize IoBC, additional criteria arise:

- **High complementarity:** To maximize IoBC, it is ideal for the absorption and EQE curves of each sub-cell to have minimal overlap, while spanning as wide a fraction of the solar spectrum as possible when combined. This complementarity maximizes both the RAINBOW to single-cell J_{sc} ratio with the minimal overlap, and the overall J_{sc} with the wide absorption span.
- **Similar maximum PCE values:** To have a large IoBC, each sub-cell within a RAINBOW combination should have similar PCE values. Note that the highest IoBC does not necessarily lead to the highest PCE.

According to the above guidelines, the perfect match for spectral splitting PV is one for which the corresponding EQE curves have similar maximum values at their respective peak wavelengths, and cover as much of the solar spectrum as possible, while keeping V_{oc} as high as possible.

2.2.2. Experimental EQE Curves

Taking these guidelines into account, we searched for possible combinations of materials for the first RAINBOW architecture

demonstration. We selected three commercially available material combinations, covering a wide-bandgap range: PBDB-T-2F:IO-4Cl,^[44] PBDB-T-2F:Y6,^[45] and PTB7-Th:COTIC-4F,^[46] the structures of which are shown in **Figure 2a**. The wide bandgap of 1.8 eV of the PBDB-T-2F:IO-4Cl blend makes it more suitable for the blue cell, as we can see from its EQE curve (Figure 2b), whereas the extremely narrow gap of 1.12 eV of PTB7-Th:COTIC-4F is more adequate for the red cell. Conversely, PBDB-T-2F:Y6, which has an intermediate gap value of 1.4 eV, can function either as the blue cell or the red cell, depending on which of the other two blends is used in the RAINBOW combination. We note that, even if the reported efficiencies of PBDB-T-2F:IO-4Cl and PTB7-Th:COTIC-4F are not amongst the highest in OPV, these materials exhibit extreme band gaps on opposite sides of the spectrum, with relatively low V_{oc} losses within organic materials, which makes them ideal to test the feasibility of the RAINBOW solar cell concept.^[44–47]

Using these materials, we manufactured and characterized well-performing solar cells, from which we obtained the current-voltage and EQE curves that were fed into the simulation model (see Section S3, Figure S8, Supporting Information). In this way, the theoretical combined efficiency was calculated for every possible RAINBOW combination between the three material blends. For a more in-depth explanation on the manufacturing and characterization procedure, the reader is referred to Experimental Section.

We first consider the wide-intermediate gap combination between PBDB-T-2F:IO-4Cl as the blue cell and PBDB-T-2F:Y6 as the red cell. As expected from their EQEs, this tandem exhibits a very modest 0.4% IoBC (Figure S7, Supporting Information). This is because the EQE curve of the blue cell (PBDB-T-2F:IO-4Cl) is entirely overshadowed by that of the red cell (PBDB-T-2F:Y6). As a result, the lower thermalization losses of the blue cell

cannot compensate its lower photocurrent, resulting in a non-functional RAINBOW combination, where the maximum combined efficiency is practically equal to that of the best performing sub-cell (the red cell).

On the other hand, the other two combinations resulted in functional RAINBOW cells, with significantly positive IoBC coefficients. In fact, the intermediate–narrow-gap combination, using PBDB-T-2F:Y6 as the blue cell and PTB7-Th:COTIC-4F as the red cell, yields a positive IoBC of 10.5% and a maximum combined efficiency of 13.7% (Figure 2b, left). In this combination, the optimal dividing wavelength range is located just below the band gap of the blue cell, most likely because of its high performance when compared with the red cell. In this case, the red cell (PTB7-Th:COTIC-4F), even with its significantly lower EQE values, is able to capture the lower energy photons that the blue cell (PBDB-T-2F:Y6) cannot absorb, resulting in a higher photocurrent for the RAINBOW combination.

Furthermore, the wide–narrow-gap combination, using PBDB-T-2F:IO-4Cl as the blue cell and PTB7-Th:COTIC-4F as the red cell (Figure 2b, right), yields the best results, showing a remarkably better maximum combined efficiency than that of either sub-cell, peaking at 10.1%, with an IoBC of 41%, and an optimal dividing wavelength range located slightly below the band gap of the blue cell. Even if the resulting combined efficiency is not amongst the highest in OPV, this combination is a remarkable example of a better final PCE due to a reduction in thermalization and absorption losses.

2.3. RAINBOW Devices

Taking into account the previous simulation results, we selected the most successful combinations and used them to validate the simulations by manufacturing and characterizing the first monolithic RAINBOW architectures using a custom-made spectral shaper setup.

2.3.1. Model Validation

To validate the simulation model we need to illuminate each sub-cell with a specific spectral fraction, measure its performance, and then repeat this measurement at every dividing wavelength. To carry out such measurements, we have developed a setup capable of generating custom light spectra that are homogeneous and can be dynamically modified with a high degree of accuracy (Figure 3a).^[40,48]

This is achieved in three steps: First, incoming light is spatially separated into all its wavelength components with a dispersive element. Second, the spatially separated beam passes through a specifically designed dynamic mask, which blocks specific wavelength components, in this case, two motorized guillotines. And last, the spectrum is recombined again into a homogeneous light spot. With the help of this contraption, we are able to generate any spectrum on-demand from a given light source (SOLS). The resulting SOLS setup can convert any solar simulator into a RAINBOW characterization station, capable of emulating the conditions of the simulations in a real measurement (Figure 3b),

in particular, the dividing-wavelength sweeps under the continuous monitoring of the solar cell parameters. We want to remark that this setup is not limited to outputting solar spectrum fractions but can deliver completely custom spectra, within the boundaries set by the input spectrum. The full description of the setup will be published elsewhere, and details can be found in references.^[40,48]

To validate the model we have chosen to perform SOLS RAINBOW measurements on the wide–narrow-gap cell combination, because of its high calculated IoBC, and its optimal dividing wavelength range that falls well within the SOLS spectral shaping capabilities. The individual SOLS characterization of the red and blue cell provides us with insights to assess the validity of the model assumptions. For the red cell (PTB7-Th:COTIC-4F) we notice that PCE behavior is mainly driven by the J_{sc} component, where the V_{oc} and FF rapidly saturate, with minor variations throughout the entire dividing wavelength range (Figure S13, Supporting Information). This behavior is consistent with the model initial assumptions (constant V_{oc} and FF), where the rapid saturation can be attributed to the relation of V_{oc} and FF with increasing illumination intensity, a phenomenon well reported in the literature.^[49–52] This saturation is likely to begin at lower light intensities in a real RAINBOW device since, due to spectral redistribution, light power density is high (spectrally concentrated) for each sub-cell (see Section S1, Figure S1, Supporting Information). We see that, above a certain light intensity threshold, the dividing wavelength dependence of these two parameters seems to play a minor role in determining the final partial efficiency of each sub-cell, being eclipsed by the dividing wavelength dependence of J_{sc} .

Intuitively, we can see that the J_{sc} of each sub-cell is proportional to the fraction width of the illuminating spectrum, as wider spectral fractions will encompass a higher amount of photons. However, we notice that for the blue cell (PBDB-T-2F:IO-4Cl), the J_{sc} slope changes suddenly after the dividing wavelength sweep surpasses 700 nm, bringing the current increase almost to a halt (Figure S14, Supporting Information). This sudden slope change can be attributed to the lack of photon absorption below 700 nm which corresponds to the band gap of PBDB-T-2F:IO-4Cl. Meanwhile, with a bandgap well below the measuring range of the SOLS setup, the PTB7-Th:COTIC-4F red cell has a J_{sc} component that constantly increases with wider spectral fractions.

By merging these two measurements as a function of the dividing wavelength, we can calculate the RAINBOW performance of the wide–narrow-gap combination (PBDB-T-2F:IO-4Cl and PTB7-Th:COTIC-4F, respectively) resulting in a high IoBC of 46.6% (Figure 3c). This high IoBC is in agreement with previous simulations and calculations, where the significant reduction of thermalization and absorption losses results in a functional RAINBOW combination. Moreover, in these measurements we also see that the optimal wavelength range is wider than the one predicted by the simulations. This could be in part due to the lack of sufficient spectral resolution in the SOLS setup, as suggested by the simulation results shown in Section S7, Supporting Information. In turn, this has important implications for the design of the optical element, where a clear separation of the wavelengths around the optimum dividing wavelength is desirable.

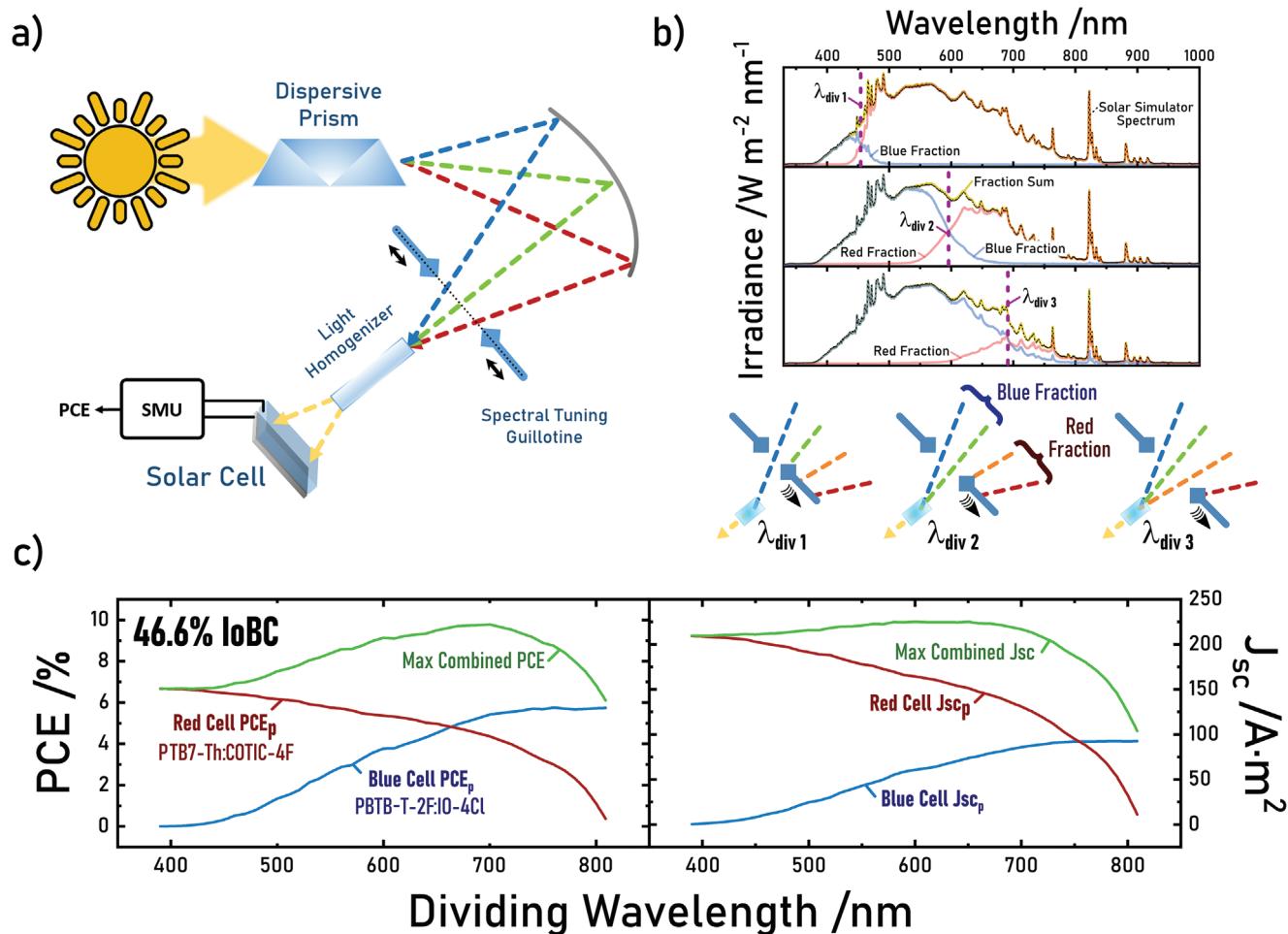


Figure 3. a) Spectrum on demand light source (SOLS) setup schematic drawing depicting its operation principle. b) Output spectra of multiple dividing wavelength conditions (top) and schematic representation of the dynamic spectral output tuning. c) Combined performance graph for PBTB-T-2F:IO-4Cl as the blue cell and PTB7-Th:COTIC-4F as the red cell measured with the SOLS setup.

2.3.2. Proof-of-Concept Device

Having validated our simulation model with the SOLS measurements we proceeded to manufacture a monolithic proof-of-concept device that includes two junctions deposited side by side, representing the simplest embodiment of a RAINBOW solar cell. To complement this two-junction proof of concept, we have also included a sketch depicting the electrical interconnections of an n-terminal RAINBOW array, as well as the top and cross-sectional view of a three-junction RAINBOW solar cell, to show that this concept can be easily scaled to any arbitrary number of junctions (Section S4, Figures S9 and S10, Supporting Information).

To manufacture the monolithic proof-of-concept device we selected the two combinations yielding the best theoretical IoBC figure of merit, that is, the wide–narrow- and the intermediate–narrow-gap combinations. To fabricate such a device on a small scale we developed a technique called partial coverage radial (PCR) spin coating, which results in a partial deposition with a well defined border within a small substrate (Figure 4a and Figure S12, Supporting Information). This technique is easy to reproduce without specialized equipment and it allows us to se-

quentially deposit multiple junctions in a single substrate with clearly defined boundaries, making it a really useful technique in RAINBOW solar cell lab scale optimization (see Section S5, Figures S11 and S12, Supporting Information).

The EQE and J - V curves of the monolithic devices were measured and fed into the numerical model to calculate the optimal dividing wavelength range and the expected maximum efficiency and IoBC coefficient (simulation results in Section S8, Figure S16, Supporting Information). In this case, instead of using the SOLS setup, to further validate the simulation results we used a more accessible solution to characterize the sub-cells: an LED based solar simulator, which consists of an array of 21 individually addressable LEDs. This setup is capable of providing homogeneous illumination with discrete fractions of the solar spectrum by varying each LED intensity. We used our simulations to set the dividing wavelength on the LED solar simulator to be as close as possible to the optimal simulated λ_{div} for each RAINBOW combination, namely at ≈ 860 and ≈ 690 nm for the intermediate–narrow- and wide–narrow-gap cell combinations respectively (Section S9, Figure S17, Supporting Information).

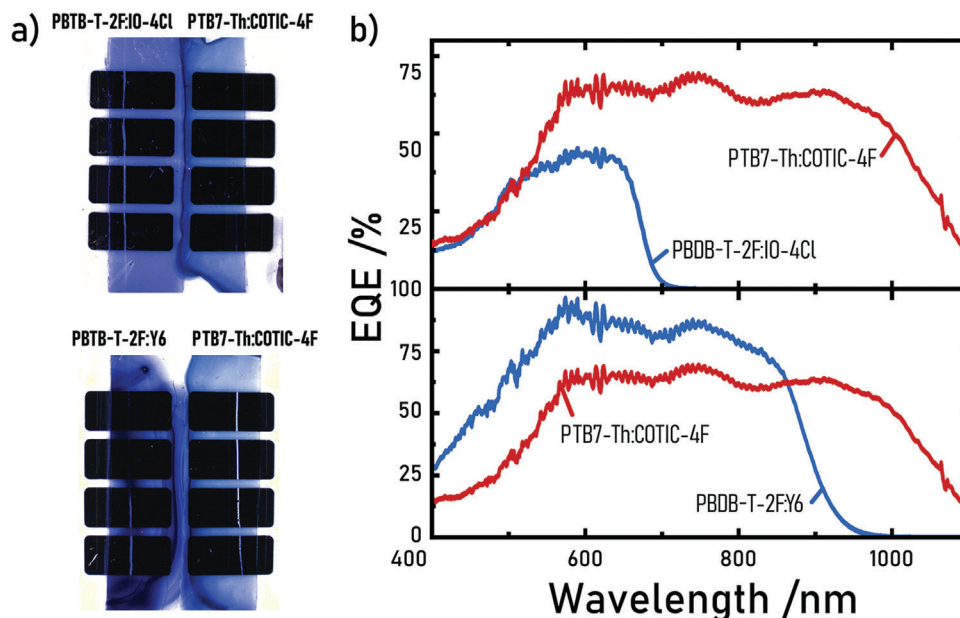


Figure 4. a) Proof-of-concept functional monolithic RAINBOW devices deposited via PCR spin coating on a single substrate. b) EQE curves of the wide–narrow-gap cell combination, that is, PBDB-T-2F:IO-4Cl as blue cell and PTB7-Th:COTIC-4F as red cell (top), and the intermediate–narrow-gap cell combination, that is, PBDB-T-2F:Y6 as blue cell and PTB7-Th:COTIC-4F as red cell (bottom) for the monolithic RAINBOW devices.

Table 1. Monolithic RAINBOW device performance, with PBDB-T-2F:IO-4Cl as the “blue cell” and PTB7-Th:COTIC-4F as the “red cell,” measured with the LED solar simulator with various spectra, simulating the behavior of the SOLS setup for a single dividing wavelength of 690 nm. The result is a combined PCE of 9.36% corresponding to 39.5% increase over the best cell (IoBC) marked with *.

Material	λ fraction	V_{oc} [V]	FF [%]	J_{sc} [$A\ m^{-2}$]	PCE [%]
PBDB-T – 2F: IO – 4Cl	Full Sun	1.20	53.6	89.2	5.75
	Blue fraction	1.20	51.8	86.0	5.32
PTB7-Th: COTIC – 4F	Full Sun	0.58	56.0	206.8	6.71
	Red fraction	0.56	60.7	119.7	4.04
RAINBOW	Combined	0.83	–	205.7	9.36
	RCoBC [%]	42.7	–	–0.5	39.5*

Table 2. Monolithic RAINBOW device performance, with PBDB-T-2F:Y6 as the “blue cell” and PTB7-Th:COTIC-4F as the “red cell,” measured with the LED solar simulator with various spectra, simulating the behavior of the SOLS setup for a single dividing wavelength of 860 nm. The result is a RAINBOW PCE of 11.5% corresponding to 12.6% increase over the best cell (IoBC) marked with *.

Material	λ fraction	V_{oc} [V]	FF [%]	J_{sc} [$A\ m^{-2}$]	PCE [%]
PBDB-T – 2F: Y6	Full Sun	0.81	60.8	241.8	11.9
	Blue fraction	0.81	61.0	223.1	11.1
PTB7-Th: COTIC – 4F	Full Sun	0.57	50.7	253.9	7.4
	Red fraction	0.54	58.6	70.9	2.3
RAINBOW	Combined	0.74	–	294.0	13.4
	RCoBC [%]	–8.0	–	21.6	12.6*

Tables 1 and **2** summarize the monolithic RAINBOW cell characterization results. The upper table section shows the J – V parameters obtained for each sub-cell under full sun illumination and using only the corresponding fraction of the solar spectrum, red or blue (see Section S9, Supporting Information). For the RAINBOW device (bottom table section), the PCE and the increase over the best cell, IoBC, are calculated from the measurements of the sub-cells following Equations (7) and (8), respectively.

The first observation is that all of the sub-cells operate with efficiencies similar to those of single-cell devices made by conventional deposition, that is, without monolithic integration (see Tables 1 and 2). For the wide–narrow-gap combination (PBDB-T-2F:IO-4Cl as the blue cell and PTB7-Th:COTIC-4F as the red cell), we have obtained an IoBC of 39.5% with a combined efficiency of 9.36% (Table 1), in good agreement with the simula-

tions in Section S8, Supporting Information which predicted an IoBC of 47.6% with a total PCE of 9.90%. For the intermediate–narrow-gap combination (PBDB-T-2F:Y6 as the blue cell and PTB7-Th:COTIC-4F as the red cell), we have obtained an IoBC of 11.5% with a combined PCE of 13.4% (Table 2), in very good agreement with the simulations of Section S8, Supporting Information, with values of 11.4% and 13.2%, respectively.

We next try to estimate the importance on these RAINBOW cells of the two main mechanisms that operate in multi-junction solar cells, that is, the reduction in the thermalization losses and the increase in absorption. In all cases, comparisons are made with respect to the best single junction amongst sub-cells for a given monolithic device. To address the changes in absorption, we use as proxy the photocurrent density. In particular, we compare the J_{sc} of the best sub-cell with that of the RAINBOW device following Equation (6). Clearly, this is only an

approximation, since, besides being proportional to the absorption, charge transport, and collection also affect the J_{sc} . In any case, as the materials and device stack being compared are the same, we use as a first approximation the changes in J_{sc} as being mainly related to changes in absorption.

On the other hand, thermalization of charges is often reflected in the energy of the extracted charges, and thus we use, again as proxy, the difference in V_{oc} between the best single junction cell and that of the RAINBOW devices. Being an N-terminal device, the V_{oc} of the latter is not well-defined. To approximate an effective, or averaged, V_{oc} for the combined cells, we need to take into account that part of the charges will be collected at the V_{oc} of the blue cell, and the rest with the V_{oc} of the red cell. A simple way of factoring this in, is by calculating the $V_{oc,comb}$ through the J_{sc} -weighted average of the corresponding sub-cell values (following Equation (9)). This expression uses the photocurrent fraction as an approximation of the P_{in} average that each sub-cell receives, and it assumes that the FF of both subcells is approximately equal.

$$V_{oc,comb} = \frac{V_{oc(red)}J_{sc(red)} + V_{oc(blue)}J_{sc(blue)}}{J_{sc,comb}} \quad (9)$$

The last two rows in Tables 1 and 2 show the parameters of the corresponding RAINBOW cells following Equations (9), (6), and (7), as well as the relative change of the combined V_{oc} , J_{sc} , and PCE with respect to the parameters for the best performing single junction cell (RCoBC). Note that the RCoBC for the PCE corresponds to the aforementioned overall figure of merit IoBC (%). While being only estimates, the RCoBC can be used to give an idea of the origin of the IoBC or, in other words, whether thermalization and/or absorption losses are reduced.

For the wide-narrow-gap combination (Table 1), the RCoBC analysis shows that this improvement basically comes from the V_{oc} RCoBC (42.7%), so in this case, the RAINBOW device does minimize thermalization losses. This is simply due to the high V_{oc} of the blue cell, which is more than twice that of the red cell.

On the other hand, for the intermediate-narrow-gap combination (Table 2) the increase in efficiency is mainly related to the large improvement in J_{sc} from the contribution of the red cell (21.6% of RCoBC), which absorbs photons well below the bandgap of the blue cell, showing a reduction on absorption losses. In fact, this even overcompensates the lower V_{oc} of the electrons extracted from the red-cell, that yield a worsening of the open-circuit voltage seen as a negative V_{oc} RCoBC (notice that the best performing cell is the blue sub-cell). Hence, this is an example of a RAINBOW combination that works well by minimizing optical absorption losses.

3. Conclusions

We have proved the feasibility of the RAINBOW solar cell multi-junction architecture which consists of a lateral (horizontal) array of solar cells, illuminated with spectrally split sunlight. The individual junctions, with distributed bandgaps, are laid out so that each sub-cell is illuminated with a wavelength range that closely matches the bandgap of the semiconductor in that particular position. The main advantages of this architecture include its relatively flat form factor, its high compatibility with roll-to-roll tech-

nologies, no stacking defect accumulation, lower active layer material consumption compared to any other multi-junction geometry, and, finally, the simple implementation of an n-terminal configuration.

Using simulations, we defined design rules for the selection of materials and devices. The RAINBOW device is optimized when choosing materials with maximum EQE value matching (rather than current matching) as well as low thermal losses particularly in the blue sub-cells. We used these criteria to select three active layer blends, namely, PBDB-T-2F:IO-4Cl, PBDB-T-2F:Y6, and PTB7-Th:COTIC-4F, with band gaps that cover a wide range of the solar spectrum. From a theoretical point of view, the efficiency increase-over-best-cell that we could obtain for two-junction cells with the selected materials span from less than 1% up to 46%. We then used a purposely made experimental setup (SOLS) that helped us to validate the simulations, thus providing a theoretical tool for material and device screening. With the SOLS setup we achieved an IoBC of close to 46% for the wide-narrow-bandgap RAINBOW combination which has PBDB-T-2F:IO-4Cl as blue cell and PTB7-Th:COTIC-4F as red cell.

Finally, we manufactured two proof-of-concept monolithic RAINBOW devices, using the here introduced partial coverage deposition technique. The combination between PBDB-T-2F:IO-4Cl and PTB7-Th:COTIC-4F yielded an IoBC of 39.5% arising from reduced thermalization losses, while RAINBOW combinations based on PBDB-T-2F:Y6 and PTB7-Th:COTIC-4F, resulted in an 11.5% IoBC, in good agreement with simulations that explain this improvement in terms of enhanced photocurrent arising from a significant reduction in absorption losses. We have also quantified the thermalization and absorption losses for each RAINBOW system, understanding the nature of the improvement in the lateral multi-junction geometry. Our results demonstrate the feasibility and significant potential of the RAINBOW concept, inviting the community to explore novel combinations, demonstrate multi-junctions with more than two sub-cells, and design efficient dispersive elements.

4. Experimental Section

Device Manufacturing: The manufacturing procedure was mainly based on spin coating, using small square substrates of $25 \times 25 \text{ mm}^2$ (except for the proof-of-concept RAINBOW devices, where substrates were $20 \times 15 \text{ mm}^2$) with an indium tin oxide (ITO) patterned front electrode. These substrates were thoroughly cleaned and ozone treated to improve wettability. On top of the patterned ITO layer, 100 μL of sol-gel ZnO solution was spin coated, which after drying was immediately annealed for 10 min at 180 $^{\circ}\text{C}$ to form a solid ZnO electron-transporting layer. The ZnO sol-gel solution was chemically synthesized using the recipe described by Tiwari et al.^[53] After this step, the substrates were placed inside the glovebox for the active layer deposition. This step was crucial in preventing oxygen and moisture-driven degradation in the sensitive photoactive materials. Active layer solutions were prepared also inside the glovebox with 1:1.5 donor-acceptor ratio at a concentration of 20 mg mL^{-1} in chlorobenzene for the PBDB-T-2F:IO-4Cl blend, at a concentration of 14 mg mL^{-1} in chloroform for the PBDB-T-2F:Y6 blend and in at a concentration of 20 mg mL^{-1} chlorobenzene with a 2% in vol% of 2-chloronaphthalene for the PTB7-Th:COTIC-4F blend. Active layers were dynamically deposited via spin coating with 60 μL droplets at various angular velocities between 800 and 3000 rpm, to manufacture a range of thicknesses. After cleaning the edges for electrode contacting, the substrates were placed inside a vacuum chamber, where 10 nm of MoO_3 and

120 nm of Ag were thermally evaporated, to serve as the hole-transporting layer and the back electrode, respectively. Subsequently, the samples were encapsulated with UV curable epoxy resin and glass cover slides, and, in the case of devices based on PBDB-T-2F:IO-4Cl, a further thermal annealing was performed at 110 °C for 10 min, resulting in a more crystalline morphology.^[44]

PCR Spin Coating: The partial spin coating deposition was achieved by statically depositing the solution in only one half of the substrate, carefully tuning the amount of liquid and the maximum angular velocity and acceleration, which resulted in a reliable coverage of only half of the substrate, leaving the other half completely untainted (Figure S11, Supporting Information). See Section S5, Supporting Information for further details regarding the different steps involved in the PCR spin coating technique as well as an assessment of the quality of the side-by-side deposition using Raman imaging.

Current–Voltage Characterization: Current–voltage (*J–V*) curves were measured using a custom-made *J–V* characterization setup, consisting of a demultiplexing board in combination with a LabVIEW application. This setup was connected to a Keithley 2400 source meter that performs high precision current and voltage measurements. To illuminate the devices, a solar simulator (XES-100S, SAN-EI Electric) was used under AM 1.5G and 1000 W m⁻² illumination. Being AAA class, this solar simulator guaranteed a homogeneous illumination area of 10 × 10 cm². The solar simulator was calibrated before each experiment to ensure the measurement reliability, using a certified reference silicon solar cell (Oriol, Newport).

Besides this, an LED solar simulator from Wavelabs (SINUS 70) was also used to generate the custom spectra for the characterization of the proof-of-concept RAINBOW devices. The spectra were achieved by modulating the different wavelength LED intensities.

A third equipment named SOLS was used, which was specially designed and fabricated for characterizing RAINBOW devices. Its functionality details are described elsewhere.^[40,48]

EQE Characterization: External quantum efficiency measurements were performed on a custom-made semi-automated experimental setup, with an associated LabVIEW controlling software. This experimental setup was coupled to a supercontinuum laser light source and a computer-controlled monochromator (LLTF contrast, Fianium) for filtering the white laser to provide a continuous spectral range. With this setup, the sample was able to be illuminated with light ranging from 400 to 1100 nm. Current measurements were made with a Keithley source meter 2450.

Raman Imaging: Raman images of monolithic devices were taken using a Witec alpha300RA piece of equipment. The samples were measured illuminating through the glass substrate by means of a 10× objective. Two different excitation wavelengths were used, namely 488 and 785 nm, with a power of ≈3 mW. The images contained 200 × 70 points, with an integration time of 0.3 s per point.

Supporting Information

Supporting Information is available from the Wiley Online Library or from the author.

Acknowledgements

The Spanish “Ministerio de Ciencia e Innovación (MICINN)” is gratefully acknowledged for its support through grant No. CEX2019-000917-S (FUNFUTURE) in the framework of the Spanish Severo Ochoa Centre of Excellence program and the AEI/FEDER(UE) grants PGC2018-095411-B-I00 (RAINBOW), TED2021-131911B-I00, and PID2021-128924OB-I00 (ISOSCELLES). The authors also thank the Catalan agency AGAUR for grant 2021-SGR-00444. M.C.V. acknowledges a FPI fellowship (PRE2019-089855) from MICINN co-financed by the European Social Fund and M.G.R. acknowledges the scholarship FPU16/02631 from the Spanish “Ministerio de Educación.” M.C.V. and M.G.R. also thank the Ph.D. programme in Materials Science from Universitat Autònoma de Barcelona in which both were enrolled. K.V. and Q.L. acknowledge funding by the European Research Council (ERC, grant agreement 864625).

Conflict of Interest

The authors declare no conflict of interest.

Data Availability Statement

The data that support the findings of this study are available from the corresponding author upon reasonable request.

Keywords

multi-junction geometries, nonfullerene blends, organic photovoltaics, RAINBOW solar cells, spectral splitting, tandem devices

Received: December 28, 2022

Revised: February 25, 2023

Published online:

- [1] S. Rühle, *Sol. Energy* **2016**, *130*, 139.
- [2] W. Shockley, H. J. Queisser, *J. Appl. Phys.* **1961**, *32*, 510.
- [3] A. D. Vos, *J. Phys. D: Appl. Phys.* **1980**, *13*, 839.
- [4] M. A. Green, *Nat. Energy* **2016**, *1*, 15015.
- [5] T. Ameri, N. Li, C. J. Brabec, *Energy Environ. Sci.* **2013**, *6*, 2390.
- [6] J. Werner, B. Niesen, C. Ballif, *Adv. Mater. Interfaces* **2018**, *5*, 1700731.
- [7] T. Ameri, G. Dennler, C. Lungenschmied, C. J. Brabec, *Energy Environ. Sci.* **2009**, *2*, 347.
- [8] M. Yamaguchi, K.-H. Lee, K. Araki, N. Kojima, *J. Phys. D: Appl. Phys.* **2018**, *51*, 133002.
- [9] B. Chen, X. Zheng, Y. Bai, N. P. Padture, J. Huang, *Adv. Energy Mater.* **2017**, *7*, 1602400.
- [10] S. Biswas, Y. J. You, P. Vincent, J. H. Bae, J. W. Shim, H. Kim, *Prog. Photovoltaics* **2020**, *28*, 946.
- [11] M. I. Hossain, W. Qarony, S. Ma, L. Zeng, D. Knipp, Y. H. Tsang, *Nano-Micro Lett.* **2019**, *11*, 58.
- [12] D. Di Carlo Rasi, R. A. J. Janssen, *Adv. Mater.* **2019**, *31*, 1806499.
- [13] W. Gao, F. Qi, Z. Peng, F. R. Lin, K. Jiang, C. Zhong, W. Kaminsky, Z. Guan, C. Lee, T. J. Marks, H. Ade, A. K. Jen, *Adv. Mater.* **2022**, *34*, 2202089.
- [14] Y. Wei, Z. Chen, G. Lu, N. Yu, C. Li, J. Gao, X. Gu, X. Hao, G. Lu, Z. Tang, J. Zhang, Z. Wei, X. Zhang, H. Huang, *Adv. Mater.* **2022**, *34*, 2204718.
- [15] Y. Cui, Y. Xu, H. Yao, P. Bi, L. Hong, J. Zhang, Y. Zu, T. Zhang, J. Qin, J. Ren, Z. Chen, C. He, X. Hao, Z. Wei, J. Hou, *Adv. Mater.* **2021**, *33*, 2102420.
- [16] NREL, Photovoltaic Research: Best Research Cell Efficiency Chart, <https://www.nrel.gov/pv/cell-efficiency.html> (accessed: April 2023).
- [17] X. Gu, X. Lai, Y. Zhang, T. Wang, W. L. Tan, C. R. McNeill, Q. Liu, P. Sonar, F. He, W. Li, C. Shan, A. K. K. Kyaw, *Adv. Mater.* **2022**, *9*, 2200445.
- [18] X. Chen, Z. Jia, Z. Chen, T. Jiang, L. Bai, F. Tao, J. Chen, X. Chen, T. Liu, X. Xu, C. Yang, W. Shen, W. E. Sha, H. Zhu, Y. M. Yang, *Joule* **2020**, *4*, 1594.
- [19] M. Bonnet-Eymard, M. Boccard, G. Bugnon, F. Sculati-Meillaud, M. Despeisse, C. Ballif, *Sol. Energy Mater. Sol. Cells* **2013**, *117*, 120.
- [20] M. Meusel, R. Adelhelm, F. Dimroth, A. W. Bett, W. Warta, *Prog. Photovoltaics* **2002**, *10*, 243.
- [21] A. Mojiri, R. Taylor, E. Thomsen, G. Rosengarten, *Renewable Sustainable Energy Rev.* **2013**, *28*, 654.
- [22] A. Mokri, M. Emziane, Beam-Splitting Versus Tandem Cell Approaches for Converting the Solar Spectrum into Electricity: A Comparative Study, International Renewable Energy Congress, Tunisia **2010**.

- [23] C. Lewis, W. Phillips, V. Shields, P. Stella, I. Bekey, in *IECEC-97 Proc. of the Thirty-Second Intersociety Energy Conversion Engineering Conf.*, IEEE, Piscataway, NJ, USA **1997**, pp. 401–406.
- [24] M. A. Smith, S. Sinharoy, V. G. Weizer, O. Khan, A. M. Pal, E. B. Clark, D. M. Wilt, D. A. Scheiman, N. Mardesich, in *Conf. Record of the IEEE Photovoltaic Specialists Conf.*, IEEE, Piscataway, NJ, USA **2000**, pp. 1139–1141.
- [25] B. Mitchell, G. Peharz, G. Siefer, M. Peters, T. Gandy, J. C. Goldschmidt, J. Benick, S. W. Glunz, A. W. Bett, F. Dimroth, *Prog. Photovoltaics* **2011**, *19*, 61.
- [26] H. Uzu, M. Ichikawa, M. Hino, K. Nakano, T. Meguro, J. L. Hernández, H. S. Kim, N. G. Park, K. Yamamoto, *Appl. Phys. Lett.* **2015**, *106*, 013506.
- [27] H. Ferhati, F. Djeflal, A. Bendjerad, A. Benhaya, A. Saidi, *Phys. E* **2021**, *128*, 114618.
- [28] S. Jiang, P. Hu, S. Mo, Z. Chen, *Sol. Energy Mater. Sol. Cells* **2010**, *94*, 1686.
- [29] H. Liang, R. Su, W. Huang, Z. Cheng, F. Wang, G. Huang, D. Yang, *Energy Convers. Manage.* **2022**, *252*, 115049.
- [30] G. Wang, Y. Yao, Z. Chen, P. Hu, *Energy* **2019**, *166*, 256.
- [31] S. A. Omer, D. G. Infeld, *Energy Convers. Manage.* **2000**, *41*, 737.
- [32] S. Mahmoudinezhad, D. T. Cotfas, P. A. Cotfas, E. J. Skjølstrup, K. Pedersen, L. Rosendahl, A. Rezanian, *Energy* **2022**, *238*, 121988.
- [33] G. Rockendorf, R. Sillmann, L. Podlowski, B. Litzenburger, *Sol. Energy* **1999**, *67*, 227.
- [34] S. M. Raupp, M. Schmitt, A. L. Walz, R. Diehm, H. Hummel, P. Scharfer, W. Schabel, *J. Coat. Technol. Res.* **2018**, *15*, 899.
- [35] D. Shin, J. Lee, J. Park, *Coatings* **2020**, *10*, 772.
- [36] A. W. Parsekian, T. A. Harris, *ACS Appl. Mater. Interfaces* **2020**, *12*, 3736.
- [37] J. Lee, J. Park, *Org. Electron.* **2020**, *83*, 105772.
- [38] F. I. Mime, M. R. Islam, E. Hossain, I. M. Mehedi, M. T. Hasan, *IEEE Access* **2021**, *9*, 40665.
- [39] I. Etxebarria, J. Ajuria, R. Pacios, *Org. Electron.* **2015**, *19*, 34.
- [40] M. Casademont-Viñas, M. Gibert-Roca, A. R. Goñi, M. Campoy-Quiles, unpublished.
- [41] S. K. Thio, S. Y. Park, *Energies* **2019**, *12*, 24.
- [42] S. D. Vorndran, S. Ayala, Y. Wu, J. M. Russo, R. K. Kostuk, J. T. Friedlein, S. E. Shaheen, C. K. Luscombe, *Proc. SPIE* **2014**, *9184*, 918423.
- [43] S. Ullbrich, J. Benduhn, X. Jia, V. C. Nikolis, K. Tvingstedt, F. Piersimoni, S. Roland, Y. Liu, J. Wu, A. Fischer, D. Neher, S. Reineke, D. Spoltore, K. Vandewal, *Nat. Mater.* **2019**, *18*, 459.
- [44] Y. Cui, Y. Wang, J. Bergqvist, H. Yao, Y. Xu, B. Gao, C. Yang, S. Zhang, O. Inganäs, F. Gao, J. Hou, *Nat. Energy* **2019**, *4*, 768.
- [45] Q. Guo, Q. Guo, Y. Geng, A. Tang, M. Zhang, M. Du, X. Sun, E. Zhou, *Mater. Chem. Front.* **2021**, *5*, 3257.
- [46] J. Lee, S. J. Ko, M. Seifrid, H. Lee, B. R. Luginbuhl, A. Karki, M. Ford, K. Rosenthal, K. Cho, T. Q. Nguyen, G. C. Bazan, *Adv. Energy Mater.* **2018**, *8*, 24.
- [47] J. Lee, S. J. Ko, H. Lee, J. Huang, Z. Zhu, M. Seifrid, J. Vollbrecht, V. V. Brus, A. Karki, H. Wang, K. Cho, T. Q. Nguyen, G. C. Bazan, *ACS Energy Lett.* **2019**, *4*, 1401.
- [48] M. Campoy-Quiles, A. R. Goñi, M. Gibert-Roca, M. Casademont-Viñas, CSIC, ES1641.1760, **2022**.
- [49] Y. Cui, H. Yao, T. Zhang, L. Hong, B. Gao, K. Xian, J. Qin, J. Hou, *Adv. Mater.* **2019**, *31*, 1904512.
- [50] R. Steim, T. Ameri, P. Schilinsky, C. Waldauf, G. Dennler, M. Scharber, C. J. Brabec, *Sol. Energy Mater. Sol. Cells* **2011**, *95*, 3256.
- [51] P. Schilinsky, C. Waldauf, J. Hauch, C. J. Brabec, *J. Appl. Phys.* **2004**, *95*, 2816.
- [52] L. J. Koster, V. D. Mihailetchi, R. Ramaker, P. W. Blom, *Appl. Phys. Lett.* **2005**, *86*, 123509.
- [53] D. C. Tiwari, S. K. Dwivedi, P. Dipak, T. Chandel, R. Sharma, in *AIP Conference Proceedings*, American Institute of Physics Inc., College Park, MD, USA **2017**.